Supplementary Information for

Double-side 2-dimensional/3-dimensional heterojunctions for inverted perovskite solar cells

Randi Azmi,[1]* Drajad Satrio Utomo,[1] Badri Vishal,[1] Shynggys Zhumagali,[1] Pia Dally,[1] Andi Muhammad Risqi,[2] Adi Prasetio,[1] Esma Ugur,[1] Fangfang Cao,[3] Imil Fadli Imran,[1] Ahmed Ali Said,[1] Anil Reddy Pininti,[1] Anand Selvin Subbiah,[1] Erkan Aydin,[1] Chuanxiao Xiao,[3,4] Sang II Seok,[2] Stefaan De Wolf[1]*

[1]King Abdullah University of Science and Technology (KAUST), KAUST Solar Center (KSC),

Physical Sciences and Engineering Division (PSE), Material Science and Engineering Program (MSE), Thuwal, 23955-6900, Kingdom of Saudi Arabia

[2]School of Energy and Chemical Engineering, Ulsan National Institute of Science and Technology (UNIST), 50 UNIST-gil, Eonyang-eup, Ulju-gun, Ulsan, 44919 Republic of Korea

[3]Ningbo Institute of Materials Technology and Engineering, Chinese Academy of Sciences, Ningbo City, Zhejiang Province, 315201, China

[4]Ningbo New Materials Testing and Evaluation Center CO., Ltd, Ningbo City, Zhejiang Province, 315201, China


*Corresponding authors: randi.azmi@kaust.edu.sa; stefaan.dewolf@kaust.edu.sa

Supplementary Table 1 | XPS analysis and coverage factors. Atomic ratio of 2PACz, HBzA, and mixture of 2PACz+HBzA onto ITO. The coverage factor can be calculated from the deconvoluted C 1s peak and In 3d5/2. The peak area of C 1s is divided by the number of atom in the molecule (2PACz and HBzA) and then divided by the In 3d5/2 core level area.

| Sample	C area	In$_3$d$_{5/2}$ area	C atoms	N / In	P / In	Coverage factor (× 10^{-3})
2PACz washed	6062.29	115223.7	14	0.16	0.09	3.76
HBzA	928.94	79197.69	7	0.11	n/a	7.52
HBzA washed	6062.29	115223.7	7	0.03	n/a	1.68
2PACz+HBzA	875.98	6213.61	21	0.12	0.15	6.71
2PACz+HBzA washed	11759.4	125488.3	21	0.09	0.16	4.46
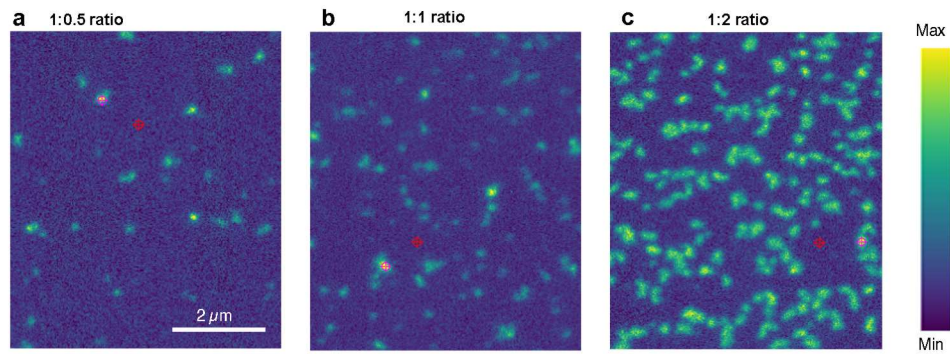
Supplementary Fig. 1 | PL mapping images of bottom-side 2D/3D films with (**a**) 1:0.5, (**b**) 1:1, and (**c**) 1:2 ratio of SAM:2D ligand at wavelength ~570 nm, which corresponds to n = 2 layers (images extracted using PHySpecV2). The bright spots indicate the 2D perovskite layer, while the dark spots belong to the 3D perovskite layer. For PL mapping measurement for bottom-side 2D passivation, we used the quartz glass to maximize the resolution of the images coupled with around 5 nm-thick ITO coating by sputtering to attach the SAM to the substrates. Then, we coated the perovskite film on top of it.
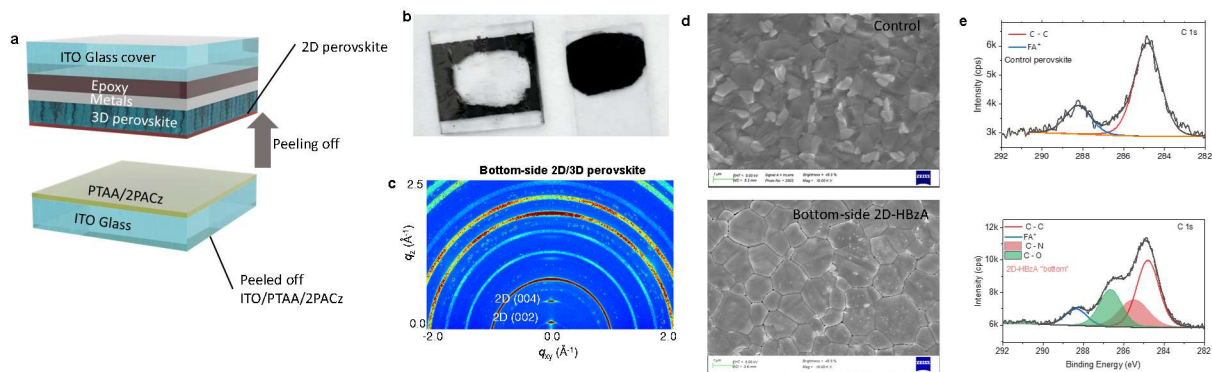
Supplementary Fig. 2 | a, Schematic of lift-off method. The peeling-off method was done by sandwiching the top surface of 2D/3D perovskite film after deposited thin metal to help the epoxy glue stick well on the perovskite film with the ITO/glass side (see schematic in panel a). After the glue is solidified, the film was peeled off from the glass/ITO/PTAA/2PACz-HTL. Then the collected perovskite film was washed with ethanol and chlorobenze dynamically to remove residual PTAA or 2PACz on the surface. Finally, the collected perovskite surface from the bottom interface is ready for characterization. **b**, Photograph of perovskite film after peeling-off. The left side is peeled-off glass, and the right side is the collected perovskite film sample. **c**, GIWAXS maps of bottom-side 2D/3D after peeling-off. The diffraction ring pattern is consistent with the result for the top-side 2D/3D sample in Fig. 2c. **d**, Top view of SEM images of the control and bottom-side 2D/3D sample after peeling off. **e**, High-resolution spectrum of the carbon region (C1s) of control and bottom-side 2D/3D perovskite films.
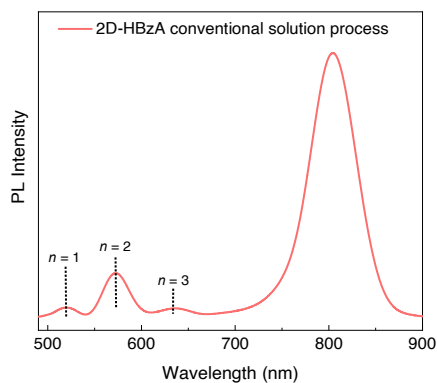

Supplementary Fig. 3 | Normalized PL of top-side 3D/2D perovskite films using a direct coating of HBzA HBr solution on top of 3D perovskite film, known as the conventional method.
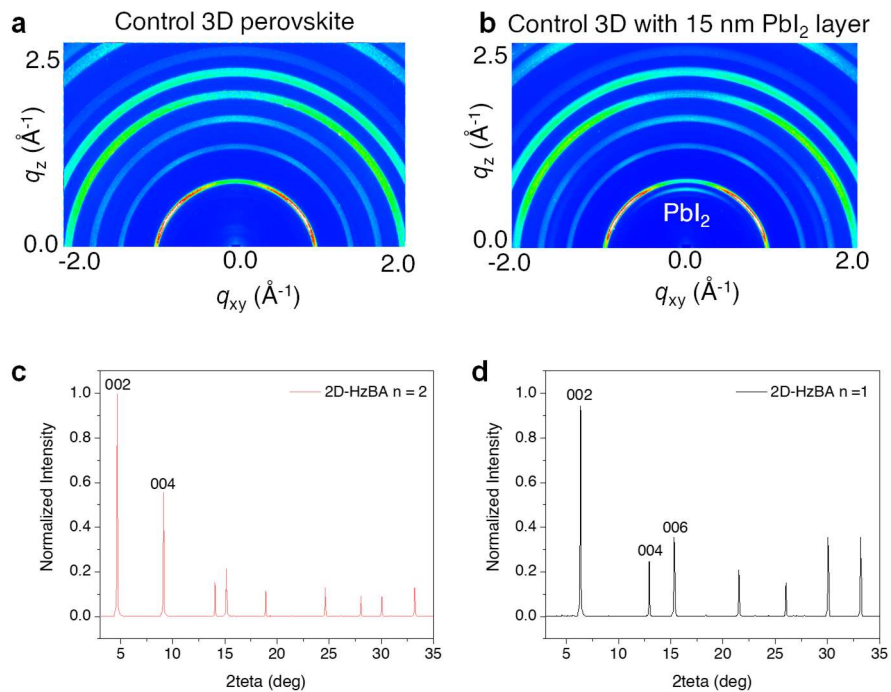
Supplementary Fig. 4 | GIWAXS maps of control 3D perovskite film before (**a**) and after the deposit of a 15 nm-thick PbI_2 layer (**b**). The strong diffraction rings at q_z = 1.0 and 1.8 Å^{-1} for both control and 2D/3D perovskite films correspond to (100) and (111) planes, respectively, featuring 3D bulk perovskite. The additional peak at ~0.9 Å^{-1} of the control film corresponds to the PbI_2 peak, confirming the deposited PbI_2 layer via vacuum deposition. X-ray diffraction spectra of a thin film of phase-pure 2D perovskite with (**c**) n = 2 and (**d**) n =1 dimensionalities.
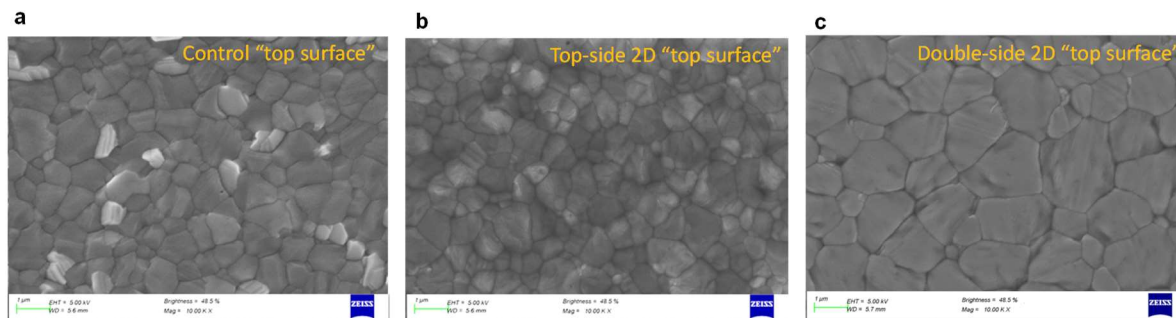
Supplementary Fig. 5 | Top view of SEM images of (**a**) control, (**b**) bottom-side 2D/3D, and (**c**) double-side 2D/3D perovskite film samples.
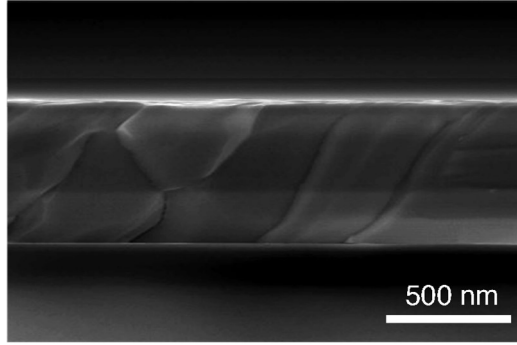
Supplementary Fig. 6 | Cross-sectional SEM image of 25 nm PbI$_2$-thick of top-side 2D/3D heterojunction sample. It is obtained that the average 2D perovskite thickness is around 55 nm.
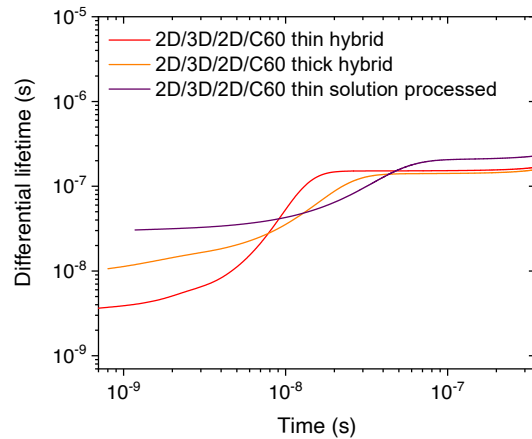
Supplementary Fig. 7 | Differential lifetime of the log-log graph from transient PL decay of at initial 100 ns of 2D/3D perovskite with different deposition methods (hybrid and conventional solution post-treatment) and thickness of 2D perovskite (35 nm and 55 nm thick) with the hybrid method, including the charge-transporting layer stacks.
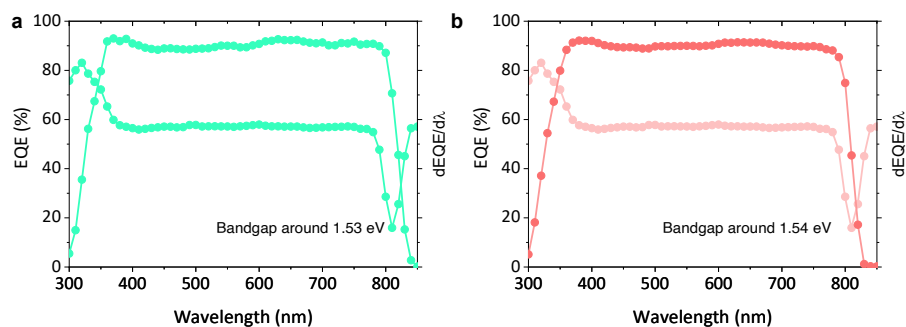
Supplementary Fig. 8 | External quantum efficiency (EQE) plot of double-side 2D/3D heterojunction-based device without white light bias and the first derivative of the EQE plot with an estimated bandgap of (**a**) $Cs_{0.025}MA_{0.075}FA_{0.90}PbI_3$ perovskite of around 1.53 eV and (**b**) $Cs_{0.05}FA_{0.95}PbI_3$ perovskite of around 1.54 eV. The measured J_{SC} values from $J\text{-}V$ analysis is consistent with the integrated J_{SC} values from the EQE analysis with only exhibit less than 1% mismatch.
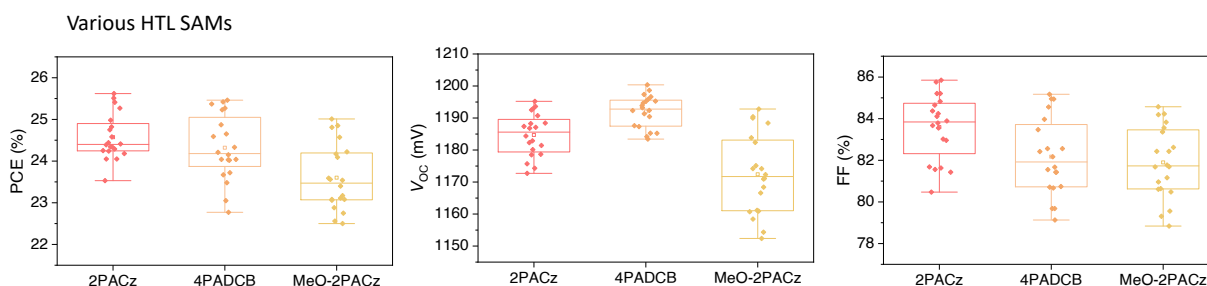
Supplementary Fig. 9 | Statistics of PCE, V_{OC}, and FF of PSCs with double-side 2D/3D heterojunctions using HBzA ligand (1:1 ratio) with various HTL SAMs (2PACz, MeO-2PACz, and 4PADCB). The statistics are obtained from 20 cells of each condition from different batches and triple-cations $Cs_{0.025}MA_{0.075}FA_{0.90}PbI_3$ perovskite.
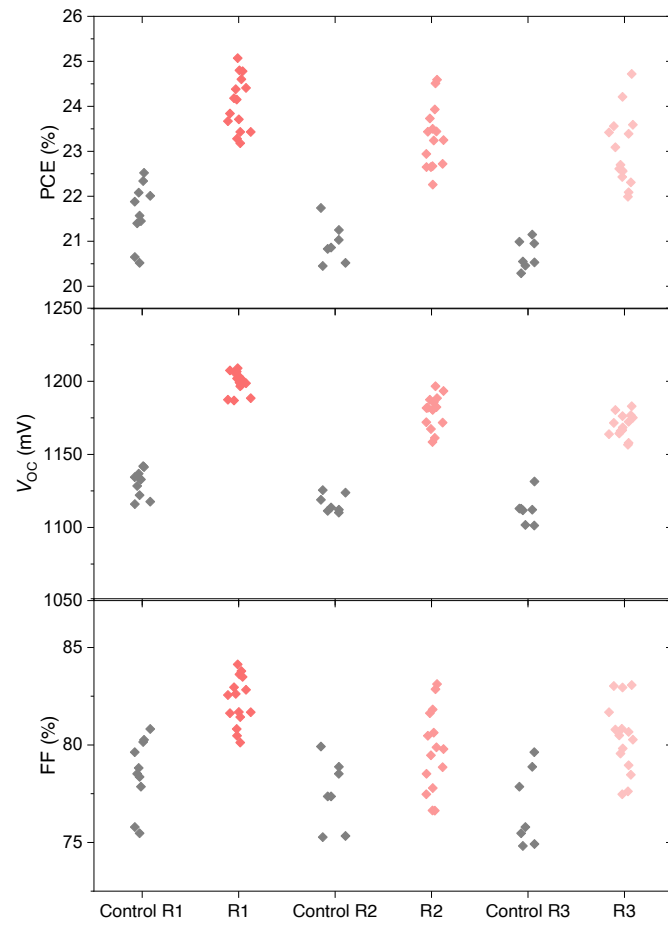
Supplementary Fig. 10 | Statistics of device performance (PCE, V_{OC}, and FF values) from person to person variation from three researchers.

ENLITECH
光焱科技股份有限公司

光焱科技光電校正實驗室
Enli Tech. Optoelectronic Calibration Lab.

測試報告
Report of Test

TAF

Testing Laboratory
3038

儀 器 名 稱 **Device Name**	Solar Cell
廠 牌 型 號 **Model No.**	Perovskite Solar Cell
儀 器 序 號 **Serial No.**	Dev-1-A
測 試 日 期 **Test Date**	2023 / 10 / 03
送 測 單 位 **Applicant**	KAUST Photovoltaic-Lab,KAUST Solar Center (KSC)
送 測 單 位 地 址 **Applicant Address**	King Abdullah University of Science and Technology (KAUST), Thuwal 23955-6900, Kingdom of Saudi Arabia

上項儀器經本實驗室量測，結果如內文。本報告含封面及內文共 6 頁，分離使用無效。

The test device is measured by the laboratory and the results are given in the content. The report consists of __6__ pages including the cover and is invalid if separated.

報告簽署人/Approved by：

日期/Date：2023. 10. 12

實驗室地址(Laboratory Address)：
高雄市路竹區路科五路 96 號 1 樓 A 區 (A area, 1F., No.96, Luke 5th Rd., Kaohsiung, Taiwan, R.O.C)

測試結果 Test Results
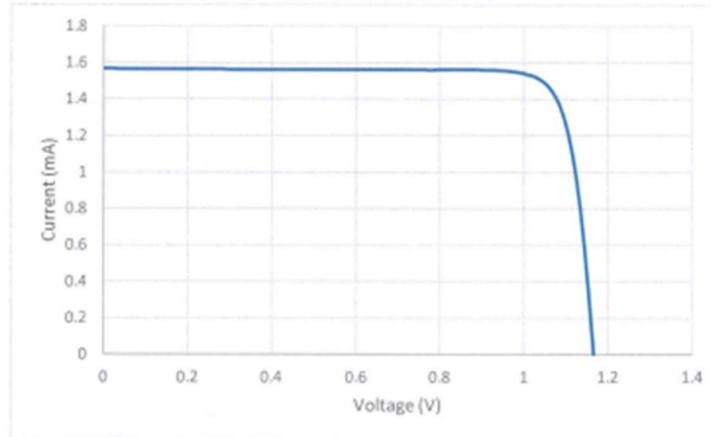
V_{OC}	=	1.167	V	±	5.138	mV
I_{SC}	=	1.565	mA	±	0.021	mA
P_{MPP}	=	1.565	mW	±	0.022	mW

V_{MPP}	=	1.035	V
I_{MPP}	=	1.512	mA
FF	=	85.72	%
Efficiency	=	25.00	%
Aperture area*	=	6.26	mm^2

Contacting method: 4-wire connection
Sweep voltage range: 1.2 V ~ -0.1 V
Sweep time: 0.65 s
Sweep direction: Voc to Isc

ENLITECH 光焱科技股份有限公司 光焱科技光電校正實驗室
Enli Tech. Optoelectronic Calibration Lab.

Report No. : PVT231001

Supporting information

儀 器 名 稱 Device Name	Solar Cell
廠 牌 型 號 Model No.	Perovskite Solar Cell
儀 器 序 號 Serial No.	Dev-1-A
測 試 日 期 Test Date	2023 / 10 / 03
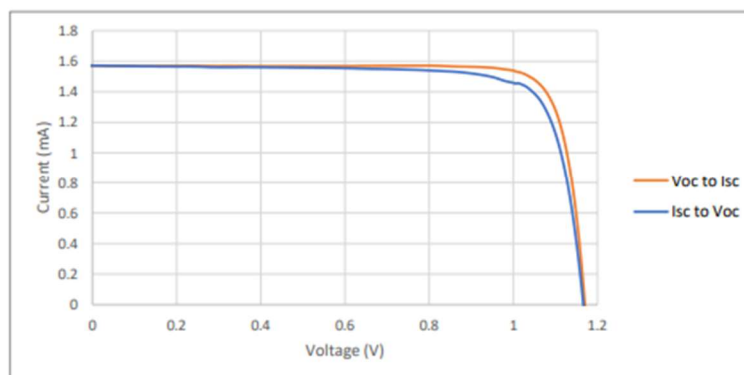
Name	Isc (mA)	Voc (V)	Pmax (mW)	Imax (mA)	Vmax (V)	Efficiency (%)	Fill Factor (%)
Dev2_Reverse	1.565	1.166	1.565	1.512	1.035	25.00	85.72
Dev2_Forward	1.566	1.165	1.452	1.398	1.034	23.27	79.55

Supplementary Fig. 11 | Certified report results from the third party of an accredited photovoltaic certification laboratory (Enli Tech. Optoelectronic Calibration Lab., Taiwan, ISO 17025 certificated). The certified PCE is 25.00% under reverse scan and 23.27% under forward scan directions with an aperture of 0.0626 cm^2 (total active area 0.1 cm^2). *The aperture masks were defined with optical microscope.
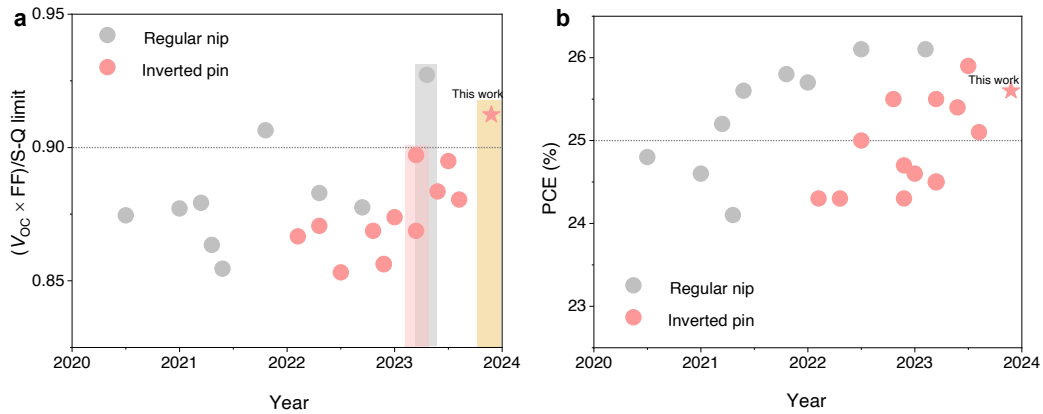
Supplementary Fig. 12 | a, $V_{OC} \times FF$ value of high efficiency of the inverted and regular structure of PSCs with respect to the Shockley–Queisser limit with PCE above 24% with bulk or top-side passivation only compared with our double-side 2D/3D passivation. **b**, PCEs of champion inverted and regular PSCs as summarized in **Supplementary Table 2**.
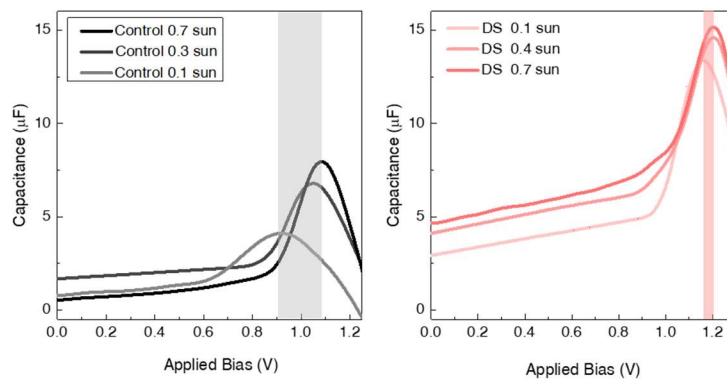
Supplementary Fig. 13 | Capacitance–voltage under various light illumination intensities of (**a**) control and (**b**) double-side 2D/3D heterojunctions-based devices. A large shifting of the V_{peak} indicated a large charge accumulation (more charge trapping) at the interfaces of solar cell devices.

Supplementary Table 2 | Summary of high performance-based inverted and regular PSCs using bulk or top-side passivation only, compared to this work with double-side passivation. The bandgap is calculated from the first derivative of the EQE plot or tau plot of absorbance of perovskite film.

Device configuration	PCE (%)	V_{OC} (V)	J_{SC} (mA cm^{-2})	FF	Bandgap (E_g)	Certified PCE (%)	Ref.
FTO/mp-TiO$_2$/FAPbI$_3$/2D/spiro-OMeTAD/Au	24.8	1.18	26.2	79.6	1.48	24.6	Science 2020, [1]
FTO/mp-TiO$_2$/FAMA/spiro-OMeTAD/Au	24.1	1.16	25.3	82.0	1.51	23.9	Nature Energy 2021, [2]
FTO/SnO$_2$/FAMA/2D/spiro-OMeTAD/Au	24.6	1.19	24.7	83.9	1.55	24.4	Nature Energy 2021, [3]
FTO/SnO$_2$/FAMA/2D/spiro-OMeTAD/Au	25.2	1.19	25.1	84.8	1.56	25.2	Nature 2021, [4]
FTO/mp-TiO$_2$/FAMA/2D/spiro-OMeTAD/Au	25.6	1.17	26.2	81.8	1.53	25.2	Nature 2021, [5]
FTO/SnO$_2$/FAMA/2D/spiro-OMeTAD/Au	25.8	1.19	25.7	83.2	1.50	25.5	Nature 2021, [6]
FTO/SnO$_2$/FAMA/2D/spiro-OMeTAD/Au	25.7	1.18	26.1	83.8	1.53	25.4	Science 2022, [7]
FTO/SnO$_2$/FAMA/2D/spiro-OMeTAD/Au	26.1	1.17	26.5	84.0	1.53	25.6	Science 2022, [8]
FTO/SnO2-KCl/FAMAPbI$_3$/2D/spiro-OMeTAD/Au	26.1	1.18	25.7	86.2	1.48	25.7	Nature 2023, [9]
ITO/2PACz/CsFAMA/2D/C$_{60}$/BCP/Ag	24.3	1.21	24.5	81.9	1.55	na	Science 2022, [10]
ITO/P3CT-N/CsFAMA/sulfur/C$_{60}$/BCP/Ag	24.3	1.19	24.8	82.9	1.55	23.5	Science 2022, [11]
ITO/PTAA/CsFAMAPbIBr/C$_{60}$/BCP/Ag	25.0	1.18	25.7	82.3	1.55	24.3	Science 2022, [12]
ITO/NiOx/CsFAMAPbIBr/PCBM/BCP/Ag	24.7	1.20	25.2	81.9	1.56	na	Energy Environ. Sci. 2022, [13]
ITO/MeO-2PACz/RbCsFAMAPbIBr/LiF/C$_{60}$/BCP/Ag	25.5	1.15	26.2	84.6	1.53	25.4	Nature 2022, [14]
ITO/2PACz/CsMAFAPbIBr/PEIE/LiF/C$_{60}$/SnOx/Ag	24.3	1.17	25.0	83.3	1.55	24.2	Joule 2022, [15]
ITO/Me-4PACz/CsFAMA/Me-4PACz/LiF/C60/BCP/Ag	24.5	1.19	24.8	83.1	1.55	na	Nature Energy 2023, [16]
ITO/MeO-2PACz/CsMAFAPbIBr/2D/C$_{60}$/BCP/Ag	24.6	1.18	24.8	84.3	1.55	24.2	Science 2023, [17]
ITO/MPA-CPA/CsMAFAPbIBr/2D/C$_{60}$/BCP/Ag	25.2	1.20	24.8	84.5	1.56	25.4	Science 2023, [18]
ITO/DMAcPA/CsFAMAPbIBr/PCBM/BCP/Ag	25.9	1.19	25.7	84.9	1.54	25.4	Nature 2023,

							[19]
ITO/NiO$_x$/PTAA/Al$_2$O$_x$/2D/CsFAPbI$_3$/PCBM/BCP/Ag	25.1	1.17	26.2	82.2	1.50	24.6	Nature Energy 2023, [20]
ITO/Me-4PACz/Al$_2$O$_3$/CsFAMAPbIBr/C$_{60}$/BCP/Ag	25.5	1.21	25.1	84.4	1.55	24.7	Science 2023, [21]
ITO/2PACz/2D/CsMAFAPbI$_3$/2D/C$_{60}$/BCP/Ag	25.6	1.19	24.9	85.9	1.53	25.0	This work

Supplementary note 1.

The first onset between the ohmic contact and the trap-induced regime is expressed as the trap limit voltage (V_{TFL}) from SCLC plots in **Extended Data Fig. 6c–d**, where the density of trap states (N_t) can be calculated following the Mott-Gurney's equation:

$$N_t = \frac{2V_{TFL}\varepsilon_0\varepsilon}{eL^2}$$

where ε_0, ε, e, and L are vacuum permittivity, perovskite dielectric constant related to the composition, elementary charge of the electron, and perovskite thickness. The relative dielectric of FAPbI$_3$ perovskite is around 47. We obtained that the double-side 2D/3D perovskite passivation films show a lower N_t for both electron- and hole-only devices (around 2.94×10^{15} cm^{-3} and 3.10×10^{15} cm^{-3}, respectively) compared to control perovskite films around 7.40×10^{15} cm^{-3}.

We also performed thermal admittance spectroscopy (TAS) to elucidate the distribution of trap states in the perovskite layers (see **Extended Data Fig. 6e**). It shows tDOS (denoted as N_t) with respect to energetic defect levels from TAS, which were obtained from the relation: $N_t (E_\omega) = -(V_{bi}.dc_\omega)/(qW k_B T.d\omega)$, where C is the capacitance, ω is the angular frequency, q is the elementary charge, k_B is Boltzmann's constant, V_{bi} is built-in voltage, and T is the temperature. This technique has been widely used and effectively quantifies the distribution of shallow and deep levels of defect in the perovskite thin films.

Supplementary References

1   Jeong, M. *et al.* Stable perovskite solar cells with efficiency exceeding 24.8% and 0.3-V voltage loss. *Science* **369**, 1615-1620 (2020). https://doi.org/10.1126/science.abb7167

2   Park, B.-w. *et al.* Stabilization of formamidinium lead triiodide α-phase with isopropylammonium chloride for perovskite solar cells. *Nature Energy* **6**, 419-428 (2021). https://doi.org/10.1038/s41560-021-00802-z

3   Jang, Y.-W. *et al.* Intact 2D/3D halide junction perovskite solar cells via solid-phase in-plane growth. *Nature Energy* **6**, 63-71 (2021). https://doi.org/10.1038/s41560-020-00749-7

4   Yoo, J. J. *et al.* Efficient perovskite solar cells via improved carrier management. *Nature* **590**, 587-593 (2021). https://doi.org/10.1038/s41586-021-03285-w

5   Jeong, J. *et al.* Pseudo-halide anion engineering for α-FAPbI$_3$ perovskite solar cells. *Nature* **592**, 381-385 (2021). https://doi.org/10.1038/s41586-021-03406-5

6   Min, H. *et al.* Perovskite solar cells with atomically coherent interlayers on SnO$_2$ electrodes. *Nature* **598**, 444-450 (2021). https://doi.org/10.1038/s41586-021-03964-8

7   Kim, M. *et al.* Conformal quantum dot-SnO$_2$ layers as electron transporters for efficient perovskite solar cells. *Science* **375**, 302-306 (2022). https://doi.org/doi:10.1126/science.abh1885

8   Zhao, Y. *et al.* Inactive (PbI$_2$)$_2$RbCl stabilizes perovskite films for efficient solar cells. *Science* **377**, 531-534 (2022). https://doi.org/doi:10.1126/science.abp8873

9   Park, J. *et al.* Controlled growth of perovskite layers with volatile alkylammonium chlorides. *Nature* **616**, 724-730 (2023). https://doi.org/10.1038/s41586-023-05825-y

10 Azmi, R. *et al.* Damp heat–stable perovskite solar cells with tailored-dimensionality 2D/3D heterojunctions. *Science* **376**, 73-77 (2022). https://doi.org/doi:10.1126/science.abm5784

11 Li, X. *et al.* Constructing heterojunctions by surface sulfidation for efficient inverted perovskite solar cells. *Science* **375**, 434-437 (2022). https://doi.org/doi:10.1126/science.abl5676

12 Li, Z. *et al.* Organometallic-functionalized interfaces for highly efficient inverted perovskite solar cells. *Science* **376**, 416-420 (2022). https://doi.org/doi:10.1126/science.abm8566

13 Huang, Y. *et al.* Finite perovskite hierarchical structures via ligand confinement leading to efficient inverted perovskite solar cells. *Energy & Environmental Science* **16**, 557-564 (2023). https://doi.org/10.1039/D2EE03355K

14 Jiang, Q. *et al.* Surface reaction for efficient and stable inverted perovskite solar cells. *Nature* **611**, 278-283 (2022). https://doi.org/10.1038/s41586-022-05268-x

15   Zhu, Z. *et al.* Correlating the perovskite/polymer multi-mode reactions with deep-level traps in perovskite solar cells. *Joule* **6**, 2849-2868 (2022). https://doi.org/https://doi.org/10.1016/j.joule.2022.10.007

16   Zheng, X. *et al.* Co-deposition of hole-selective contact and absorber for improving the processability of perovskite solar cells. *Nature Energy* **8**, 462-472 (2023). https://doi.org/10.1038/s41560-023-01227-6

17   Li, G. *et al.* Highly efficient p-i-n perovskite solar cells that endure temperature variations. *Science* **379**, 399-403 (2023). https://doi.org/doi:10.1126/science.add7331

18   Zhang, S. *et al.* Minimizing buried interfacial defects for efficient inverted perovskite solar cells. *Science* **380**, 404-409 (2023). https://doi.org/doi:10.1126/science.adg3755

19   Tan, Q. *et al.* Inverted perovskite solar cells using dimethylacridine-based dopants. *Nature* **620**, 545-551 (2023). https://doi.org/10.1038/s41586-023-06207-0

20   Li, H. *et al.* 2D/3D heterojunction engineering at the buried interface towards high-performance inverted methylammonium-free perovskite solar cells. *Nature Energy* **8**, 946-955 (2023). https://doi.org/10.1038/s41560-023-01295-8

21   Peng, W. *et al.* Reducing nonradiative recombination in perovskite solar cells with a porous insulator contact. *Science* **379**, 683-690 (2023). https://doi.org/doi:10.1126/science.ade3126